

Article

An Investigation on Flame Shape and Size for a High-Pressure Turbulent Non-Premixed Swirl Combustion

Zhongya Xi ^{*}, Zhongguang Fu, Xiaotian Hu, Syed Waqas Sabir  and Yibo Jiang

National Thermal Power Engineering & Technology Research Center, North China Electric Power University, Beijing 102206, China; fzg@ncepu.edu.cn (Z.F.); huxt@ncepu.edu.cn (X.H.); engr.waqasshah@hotmail.com (S.W.S.); jiangyb@ncepu.edu.cn (Y.J.)

^{*} Correspondence: xizhongya@ncepu.edu.cn; Tel.: +86-10-6177-2361

Received: 13 March 2018; Accepted: 10 April 2018; Published: 13 April 2018



Abstract: Flame shape and size for a high-pressure turbulent non-premixed swirl combustion were experimentally investigated over a wide range of varying parameters including fuel mass flow rate, combustor pressure, primary-air mass flow rate, and nozzle exit velocity. A CFD simulation was conducted to predict the flame profile. Meanwhile, a theoretical calculation was also performed to estimate flame length. It was observed that flame length increased linearly with increasing fuel mass flow rate but decreased with the increment of combustor pressure in the power function. The flame diminished at a larger primary-air mass flow rate but remained unaffected by the increasing nozzle exit velocity. Considering the global effect of all parameters at a particular pressure, the flame length generally decreased as the primary-air to fuel ratio increased. This was attributed to the reduced air entrainment required to dilute the fuel to stoichiometric proportions. The CFD simulation offered a good prediction of the variation trends of flame length, although some deviations from experimental values were observed. The theoretical calculation estimated the trends of flame length variation particularly well. Nevertheless the difference between the theoretical and experimental results was found to be due to the swirl influence. Hence, a swirl factor was proposed to be added to the original equation for swirl flames.

Keywords: flame shape and size; high-pressure non-premixed swirl flame; effects of operating conditions; CFD numerical simulation; theoretical calculation

1. Introduction

Flame shape and size are crucial parameters, which have to be carefully considered when designing and operating a combustion device since they determine many combustion features, e.g., the temperature field, pollutant emission, combustion efficiency, and material safety.

Turbulent non-premixed flame geometric properties have been investigated extensively. Various geometrical characteristics considered in the present investigation include flame shape, flame length L_f [1], flame width w [2,3], flame center and flame center length L_c [4–6]. In particular, L_f is given primary consideration relative to other flame aspects. The flame dimensions are defined as shown in Figure 1. Classically, flame length L_f is determined as the distance between the burner exit and the axis point of the stoichiometric line. For an over-ventilated flame where more than a stoichiometric oxidizer is supplied in the surroundings to burn the fuel continuously, L_f can be described by Equation (1)

$$\Phi(r = 0, x = L_f) = 1 \quad (1)$$

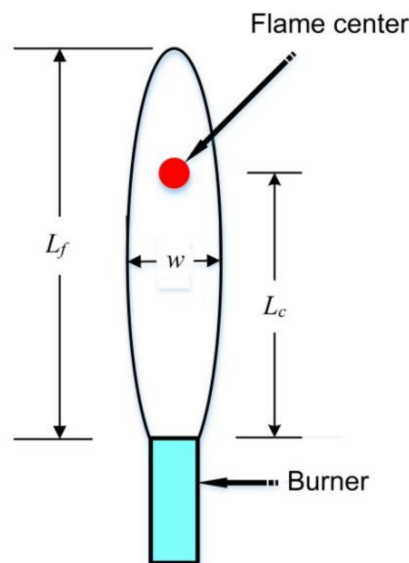


Figure 1. Flame size and position schematic diagram.

Flame width w is the stoichiometric width at its broadest section, i.e., maximum flame diameter. The flame center is applied to consider intensively the flame position as a point, which is calculated using the concept of gravity center. For calculating the gravity center, each pixel is considered as a local position, and the intensity of each pixel represents its mass. The same mathematical method is used to determine the flame center. The flame position is indicated by the flame center length L_c , which is defined as the distance between the flame center and the injection nozzle exit.

Interest in being able to interpret and estimate turbulent jet flame length has a long history. The earliest studies were derived from those of Hottel [7], Hawthorne et al. [8], and Wohl et al. [9] reported in the late 1940s and early 1950s. Major reviews of this topic were performed by Becker and Liang [10], Delichatsios [11], and Blake and McDonald [12].

In recent decades, Chen and Driscoll [13] studied flame length for swirl intensity; it was found that L_f has a different scaling in swirl flames than for simple jet flames. Swirl flame length shortens significantly in comparison to flame with no swirl, due to the enhanced fuel-air mixing rate caused by the addition of swirl. Peters and Götting [14] derived approximate solutions for large buoyant jet diffusion flames into still and horizontally co-flowing air. They obtained a closed form solution for the L_f of vertical flames as a function of the Froude number. It was concluded that, in the buoyancy-controlled regime, their expression yields asymptotically a Froude number dependence of $Fr^{1/5}$, which is in good agreement with measurements. While for the momentum-controlled regime, L_f is independent of Froude number. Røkke et al. [15] experimentally investigated L_f of unconfined turbulent partially premixed propane/air flames; the results revealed that L_f has a strong dependence on the ratio of the nozzle outlet velocity to the outlet diameter, the Froude number, and the fuel mass fraction. Mei et al. [16] studied the effects of coflow velocity on flame shape and size by performing CFD calculation. Giorgi et al. [17] observed the flame structure for an inverse diffusion combustion with a chemiluminescence emission method. Wang et al. [18] examined the evolution of the flame length of a buoyant jet diffusion flame restricted by parallel sidewalls at reduced pressure; they pointed out that the flame length at decreased pressure is found to be slightly longer than that at normal pressure.

The main factors affecting turbulent flame length are (a) the flame Froude number, Fr_f , (b) the stoichiometric mixture fraction, f_s , (c) the ratio of nozzle fluid to ambient gas density, ρ_e/ρ_∞ , (d) the

initial jet diameter, d_j . Based on the analysis presented by Delichatsios [11] and Bahadori et al. [19], a global flame Froude number can be expressed as Equation (2):

$$Fr_f = \frac{v_e f_s^{3/2}}{\left(\frac{\rho_e}{\rho_\infty}\right)^{1/4} \left[\frac{T_f - T_\infty}{T_\infty} g d_j\right]^{1/2}} \quad (2)$$

where ρ_e is the density of nozzle fluid, and ρ_∞ is the ambient fluid density. T_f represents the flame temperature, which is approximately equal to the adiabatic flame temperature T_{ad} while T_∞ is the ambient fluid temperature. Moreover, g is the acceleration of gravity, d_j is the nozzle exit diameter, and v_e is the nozzle exit velocity, which is calculated by Equation (3)

$$v_e = \frac{\dot{m}_e}{\rho_e \pi d_j^2 / 4} \quad (3)$$

where \dot{m}_e stands for the mass flow rate of nozzle fluid.

The stoichiometric mixture fraction, f_s is calculated by Equation (4).

$$f_s = \frac{1}{(\dot{m}_{air} / \dot{m}_{fuel})_{stoic} + 1} \quad (4)$$

where \dot{m}_{air} stands for air mass flow rate, \dot{m}_{fuel} stands for fuel mass flow rate, and the subscript stoic represents stoichiometric.

The flame Froude number Fr_f is used to characterize the relative importance of the initial jet momentum flux and buoyant forces acting on the flame. For smaller values of Fr_f , the flame is controlled by buoyancy, which is caused by significant density differences produced during combustion. While for larger values, the initial jet momentum dominates the mixing as well as the velocity field within the flame.

The combined impact of the above four primary factors on flame length is given by Equations (5) and (6) corresponding to two regimes respectively [11].

For a buoyancy-controlled regime, $Fr_f < 5$

$$L_f = 13.5 \frac{Fr_f^{2/5} (\rho_e / \rho_\infty)^{1/2} d_j}{\left(1 + 0.07 Fr_f^2\right)^{1/5} f_s} \quad \text{for } Fr_f < 5 \quad (5)$$

For a momentum- controlled regime, $Fr_f \geq 5$

$$L_f = 23 \frac{(\rho_e / \rho_\infty)^{1/2} d_j}{f_s} \quad \text{for } Fr_f \geq 5 \quad (6)$$

It should be noted that in Equation (6), i.e., for momentum-dominated flame, L_f does no longer vary with Fr_f , so Fr_f is not included in this equation.

Some analysis based on theoretical Equations (5) or/and (6) are presented as follows. Choudhuri and Gollahalli [20] performed an investigation on flame length for hydrogen–hydrocarbon composite fuel turbulent jet flames. They found that the numerically predicted flame length showed a similar trend to experimental ones, although the predicted values were higher than the measured values by a factor of approximately 1.4. Yang and Blasiak [21] numerically studied the influences of oxygen concentration, oxidizer temperature, fuel temperature, fuel flow rates, and fuel nozzle diameter on the flame volume and size. They derived a simple correlation of the flame length and volume relative to the flow parameters for the high-temperature air combustion condition. Kim et al. [22] proposed a modified correlation between dimensionless flame lengths and a flame Froude number to estimate L_f for the two kinds of oxy-fuel combustors. Hu et al. [23] measured flame length at a reduced

atmospheric pressure for turbulent buoyant jet diffusion flames; it was reported that the normalized L_f was longer in the lower pressure atmosphere. The flame length data was successfully collapsed with theory, although a factor of 0.8 was required globally to include influences of decreased entrainment and increased fluctuation at lower pressure.

In our investigation, flame shape and size for a high-pressure turbulent swirl non-premixed flame were studied experimentally and numerically under various operating conditions. These varying conditions include fuel flow rate \dot{m}_F , combustor pressure P , primary air flow rate \dot{m}_{pri} , and nozzle exit velocity v_e . Meanwhile, a theoretical calculation for L_f was also performed to obtain its prediction performance by comparing with measurements.

2. Experimental Setup

2.1. Experimental Apparatus

For this study, a 20 kW high-pressure combustion test facility was installed, which mainly consists of three sections, as displayed in Figure 2.

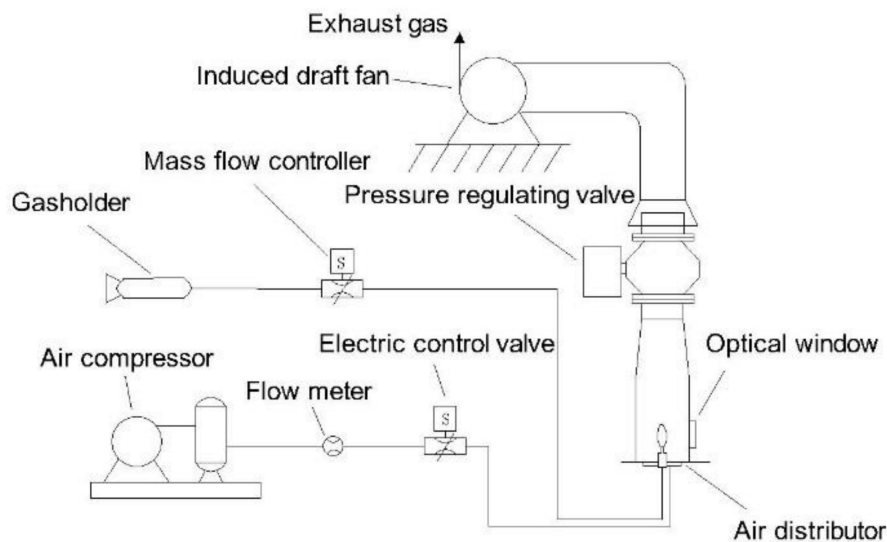


Figure 2. High-pressure combustion test rig schematic diagram.

- (1) The supply section, where fuel (methane) is supplied with a gasholder. The fuel is controlled and measured with a mass flow controller VF-100-SONARtrac, with a maximum fuel mass flow rate of 36 g/min. Air is provided by an air compressor, which has a maximum total air mass flow rate of 2.5 kg/min. The air mass flow rate is regulated using an electric control valve EV-25PCUN40RPF and measured with an air flow meter LUGB-2405-P4.
- (2) The combustion chamber, which is an axisymmetric cylindrical chamber, has a diameter of 0.3 m and height of 1.35 m, as displayed in Figure 3. This combustion chamber is primarily composed of four components: swirl injector, wind distributing plate, annular cooling slot close to the inner wall, and combustor. The swirl injector is employed for improving mixing quality, as shown in Figure 4. A portion of air flows tangentially through a radical swirler to carry fuel supplied by a central fuel nozzle into the combustor where combustion occurs. This portion of air is called primary air. The methane and primary air mix with each other partially in the injector sector; this mixing degree is not complete as the distance where mixing can occur is relatively short. The rest of the air flows through small holes in the air distributing plate and annular slot close to the inner wall. This air cools the metal material, thus, avoiding heat damage and then blends with the combustion gas. There is an optically accessible window mounted on the combustor wall, which is employed to record the flame zone.

- (3) The exhaust section consists of two components: a pressure regulating valve and an induced draught system. The pressure regulating valve controls the combustor operating pressure. The induced draught system is applied to induce exhaust gas to the atmospheric environment.

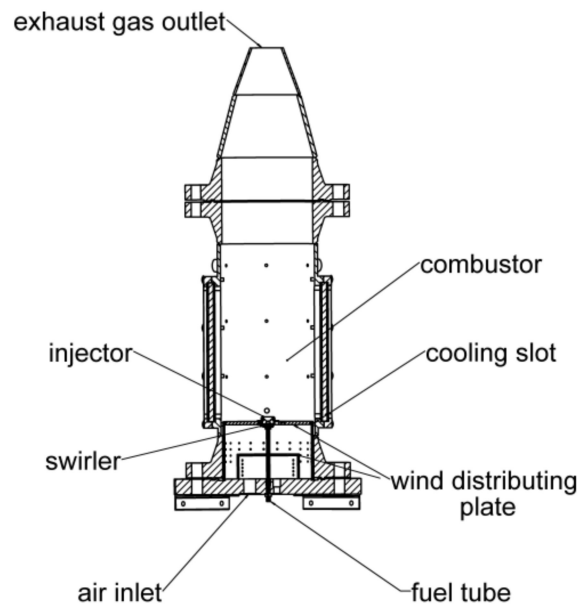


Figure 3. The combustion chamber.

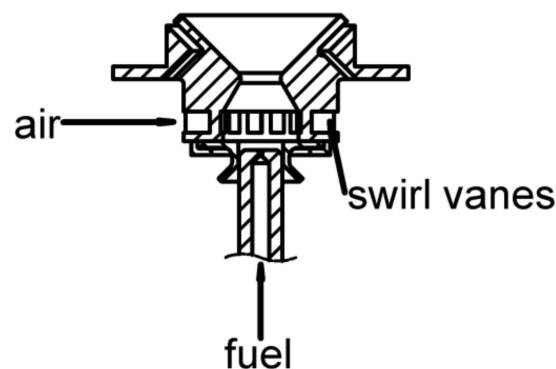


Figure 4. Swirl injector.

2.2. Measurement Methods

To determine the location of flame zone, CO_2^* chemiluminescence was used [24–26], where the asterisk refers to electronically-excited molecules. As an indicator of the reaction zone, the formation of CO_2^* contains three elementary steps in Equation (7) [24].



The first step is a three-body reaction, which indicates the production of CO_2^* . Afterward, CO_2^* returns to the ground state through the second and third step. The second step reaction is responsible for the emission of light by CO_2^* and competes with the third step reaction which is a quenching step.

The flame shape was acquired by recording the CO_2^* chemiluminescence image through the optical window, using a high-speed camera (Olympus *i* speed 3) coupled to a band filter (BG 38)

with a bandwidth of 340–600 nm, as shown in Figure 5. The recording frame rate was 400 frames per second, and a total of 800 consecutive frames were averaged to obtain an averaged flame image at each condition, which was then used to analyze the flame shape and size.



Figure 5. Flame measuring instruments: (a) high-speed camera; (b) optical filter.

2.3. Experimental Conditions

For the convenience of analyzing, the primary air \dot{m}_{pri} (which is the air through the swirl burner) was calculated. As shown in Figure 6, a 3D CFD cold simulation (total air = 0.05 kg/s, not the test condition in the present work) revealed that the primary air \dot{m}_{pri} was 0.05 times of the total air by mass flow rate \dot{m}_A , and this relation remained unchanged for various operating conditions, i.e., $\dot{m}_{pri} = 0.05 \dot{m}_A$.

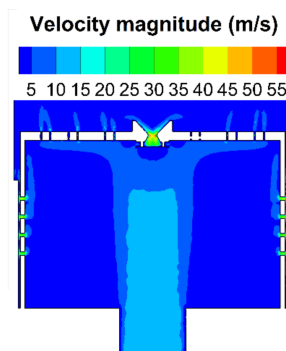


Figure 6. Velocity magnitude at center plane from a 3D CFD result.

To investigate the influence of the operating conditions on flame shape and size, test cases were classified into three categories, as shown in Table 1. Case I was used to study: (i) the effect of fuel mass flow rate \dot{m}_F at a fixed \dot{m}_A under different combustor pressures P ; and (ii) the effect of combustor pressure P (4–6 bar) at a fixed \dot{m}_F and \dot{m}_A . Case II was used to study the effect of the primary air mass flow rate \dot{m}_{pri} at a given \dot{m}_F . Case III was used to study the effect of the nozzle exit velocity v_e at a nearly constant \dot{m}_{pri}/\dot{m}_F , where v_e is calculated by Equation (3).

Table 1. Test conditions.

Case	Combustor Pressure, P (bar)	Fuel Mass Flow Rate, \dot{m}_F (g/min)	Air Mass Flow Rate, \dot{m}_A (kg/min)	Primary Air, \dot{m}_{pri} (g/min)	\dot{m}_{pri}/\dot{m}_F	Nozzle Exit Velocity, v_e (m/s)	
I	1	4	8	1.7	85	10.6	3.73
	2	4	10	1.7	85	8.5	3.73
	3	4	12	1.7	85	7.1	3.73
	4	5	8	1.7	85	10.6	2.98
	5	5	10	1.7	85	8.5	2.98
	6	5	12	1.7	85	7.1	2.98
	7	6	8	1.7	85	10.6	2.49
	8	6	10	1.7	85	8.5	2.49
	9	6	12	1.7	85	7.1	2.49
II	10	5	16	1.7	85	5.3	2.98
	11	5	16	1.8	90	5.6	3.16
	12	5	16	1.9	95	5.9	3.33
	13	5	16	2.0	100	6.3	3.51
	14	5	16	2.1	105	6.6	3.69
	15	5	16	2.2	110	6.9	3.86
III	16	5	8	1.3	65	8.1	2.28
	17	5	10	1.6	80	8.0	2.81
	18	5	12	1.9	95	7.9	3.33
	19	5	14	2.2	110	7.9	3.86
	20	5	16	2.5	125	7.8	4.39

3. CFD Simulation Setup

A CFD steady calculation was conducted using the commercial software FLUENT 6.3 (ANSYS, Canonsburg, PA, USA). For detailed descriptions on the fundamental conservation equations of mass, momentum, and energy, please refer to the FLUENT 6.3 help documents [27]. As the actual 3D geometry of the combustor is very complicated, the numerical simulation was performed using a 2D axisymmetric model to reduce computational cost, as displayed in Figure 7. In this 2D model, some simplifications were employed for the ease of calculation. The holes in the distributing plate were omitted, as the air through them is minute. Air enters into the combustor from two annular inlets, air inlet 1 and air inlet 2, where the air through inlet 1 is the primary air. The swirler was also omitted. Instead, the swirl was simulated by defining the air flow direction of inlet 1 when setting the boundary conditions. The mesh consisted of 39,435 quadrilateral cells over the whole computational domain. Finer grids were generated particularly in the regions near the fuel nozzle, air inlet, and flame axis. Additionally, another refined mesh consisting of 72,863 quadrilateral cells was generated for verifying the grid-independency of the predicted results. The verification results are displayed in Figure 8; one can see that the temperature fields and CO₂ mass fractions for Case 1 using two distinct cells are kept at high consistency, which means the simulation result no longer changes with the increasing mesh cells. Therefore the 39,435 cells mesh scheme was used for simulating the rest of the other cases.

The realizable k - ϵ turbulence model with standard wall function was used as a viscous model. The eddy dissipation model (EDM) [27,28] was considered as a combustion model. This model is based on the mixed-is-burned approximation, which is usually acceptable for non-premixed flames, where turbulence slowly mixes fuel and oxidizer into the reaction zones in which they burn quickly. This approximation assumes that combustion is mixing-limited, allowing neglect of the complicated chemical kinetic rates and assuming instantaneous ignition upon mixing. With EDM, the net rate of production of species i due to reaction r , $R_{i,r}$ is determined by the smaller (that is, the limiting value) of the two Equations (8) and (9)

$$R_{i,r} = v'_{i,r} M_{w,i} Ap \frac{\epsilon}{k} \min_{\mathfrak{R}} \left(\frac{Y_{\mathfrak{R}}}{v'_{\mathfrak{R},r} M_{w,\mathfrak{R}}} \right) \quad (8)$$

$$R_{i,r} = v'_{i,r} M_{w,i} A B \rho \frac{\epsilon}{k} \frac{\sum_P Y_P}{\sum_j v''_{j,r} M_{w,j}} \quad (9)$$

where Y_P stands for the mass fraction of any product species P , $Y_{\mathfrak{R}}$ stand for the mass fraction of a particular reactant \mathfrak{R} , A is an empirical constant equal to 4.0, and B is an empirical constant equal to 0.5.

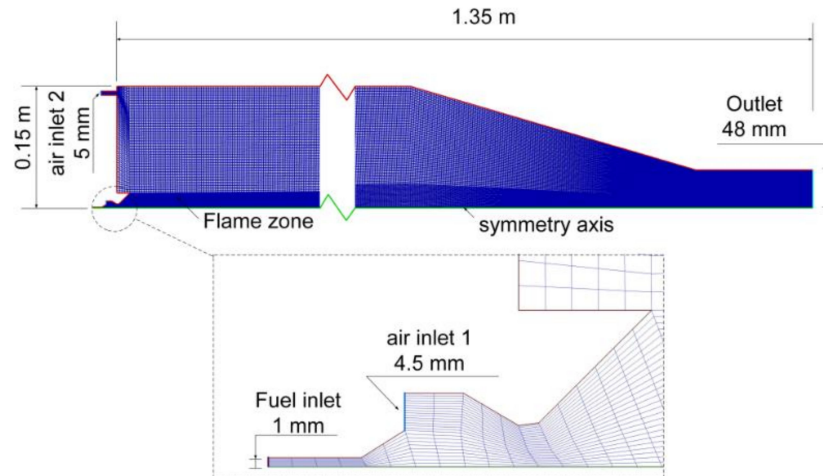


Figure 7. CFD geometry and mesh.

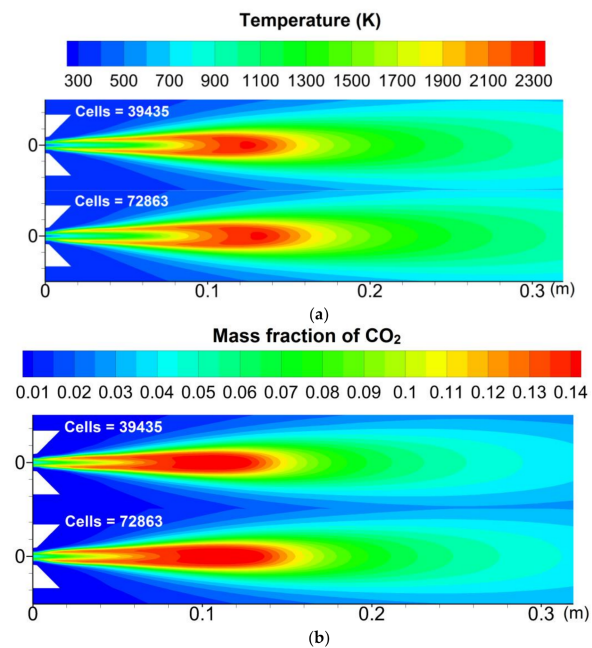


Figure 8. The verification of grid-independency: (a) flame temperature field; (b) CO₂ mass fraction.

To calculate the flame zone, the simple one-step methane–air global reaction was used. As a product of this reaction, the CO₂ mass fraction field in the simulation result was considered as a numerical flame zone. The discrete ordinate radiation model (DO) with a weighted sum of the gray gas model (WSGGM) was employed as a radiation model.

As for the boundary conditions, the fuel inlet, air inlet 1, and air inlet 2 were set to mass flow inlets. The mass flow rate of air inlet 1 is \dot{m}_{pri} , as shown in Table 1. The mass flow rate of inlet 2 is

the difference between \dot{m}_A and \dot{m}_{pri} , i.e., $\dot{m}_A - \dot{m}_{pri}$. A flow direction vector was defined to simulate the swirl of air inlet 1, where the axial-component, radial-component and tangential-component of the flow direction were 1, 0 and 0.7 respectively, according to the corresponding 3D CFD calculation results. The outlet was set to the pressure outlet; the wall was set to adiabatic boundary conditions, as negligible heat transfers to the surrounding due to its low temperature resulting from the cold air through air inlet 2. The pressure-velocity coupling was solved using the SIMPLE algorithm, and the convective terms in all governing equations were discretized using the second-order upwind scheme.

4. Results and Discussion

4.1. Theoretical Results of Flame Length

For the sake of convenience and simplicity of computation in the present situation, the mixture of fuel and primary air is regarded as a nozzle exit fuel mixture \dot{m}_e . This simplifies the calculation of f_s with Equation (4) which is then used to estimate flame length with theoretical Equations (5) or (6) for all cases. Thus, with changing methane or primary air at different conditions, distinct fuel mixtures are produced which have different f_s . It should be noted that the mixing degree of mixture fuel depends upon the level of mixing achieved within the nozzle convergent section. The density of nozzle exit mixture fuel ρ_e remained nearly equal to ambient air density ρ_∞ , i.e., $\rho_e = \rho_\infty = \rho_A$ since the percentage of primary air \dot{m}_{pri} in the nozzle fluid was more than 84% for all cases. The nozzle throat, as shown in Figure 4, is considered as the nozzle injection exit with a diameter of 0.01 m, i.e., $d_j = 0.01$ m. Therefore, L_f is the distance between the flame tip and nozzle throat. The T_f for all measured flames is approximately 2300 K (obtained in CFD results), and T_∞ is 288 K. v_e is obtained by Equation (3), where $\dot{m}_e = (\dot{m}_F + \dot{m}_{pri})/60,000$.

The results of L_f with theory calculation are shown in Table 2; one can see that the values of Fr_f for all cases are smaller than 5, which indicates that buoyancy dominates the flame. Therefore Equation (5) was used to estimate the flame length for all cases. The results of theoretical L_f are plotted to compare with the experimental and numerical L_f in the next sections to determine the theoretical prediction performance.

Table 2. The theoretical result of flame length.

Case	P (bar)	\dot{m}_F (g/min)	\dot{m}_A (kg/min)	\dot{m}_{pri} (g/min)	\dot{m}_{pri}/\dot{m}_F	v_e (m/s)	ρ_A (kg/m ³)	f_s	Fr_f	L_f (cm)
1	4	8	1.7	85	10.6	3.73	4.84	0.639	2.303	18.4
2	4	10	1.7	85	8.5	3.73	4.84	0.522	1.702	24.3
3	4	12	1.7	85	7.1	3.73	4.84	0.444	1.336	28.6
4	5	8	1.7	85	10.6	2.98	6.05	0.639	1.843	19.6
5	5	10	1.7	85	8.5	2.98	6.05	0.522	1.361	24.4
6	5	12	1.7	85	7.1	2.98	6.05	0.444	1.068	27.8
7	6	8	1.7	85	10.6	2.49	7.26	0.639	1.536	20.0
8	6	10	1.7	85	8.5	2.49	7.26	0.522	1.134	23.9
9	6	12	1.7	85	7.1	2.49	7.26	0.444	0.890	26.8
10	5	16	1.7	85	5.3	2.98	6.05	0.347	0.737	32.6
11	5	16	1.8	90	5.6	3.16	6.05	0.364	0.839	32.2
12	5	16	1.9	95	5.9	3.33	6.05	0.381	0.949	31.6
13	5	16	2	100	6.3	3.51	6.05	0.398	1.068	31.0
14	5	16	2.1	105	6.6	3.69	6.05	0.416	1.194	30.2
15	5	16	2.2	110	6.9	3.86	6.05	0.433	1.330	29.4
16	5	8	1.3	65	8.1	2.28	6.05	0.501	0.980	24.2
17	5	10	1.6	80	8.0	2.81	6.05	0.495	1.181	25.4
18	5	12	1.9	95	7.9	3.33	6.05	0.490	1.384	26.0
19	5	14	2.2	110	7.9	3.86	6.05	0.487	1.586	26.2
20	5	16	2.5	125	7.8	4.39	6.05	0.484	1.789	26.0

4.2. Effects of Fuel Mass Flow Rate

Figure 9 shows the experimental and CFD flame images for fuel mass flow rate \dot{m}_F under varying combustor pressures P in Case I (Case 1–9). Note that the experimental flame base is the nozzle divergent end, so the measured flame size shown in images (a), (c), and (e) needs to be summed up

with the distance between the nozzle divergent end and the throat to obtain the experimental L_f since the throat is regarded as the nozzle injection exit. One can see that the experimental flame shape elongates and widens as \dot{m}_F increases at a fixed P , which is explained by the increase in axial and radial diffusion of the fuel at higher \dot{m}_F . The CFD results agreed well with the measurements in the variation trends of flame appearance.

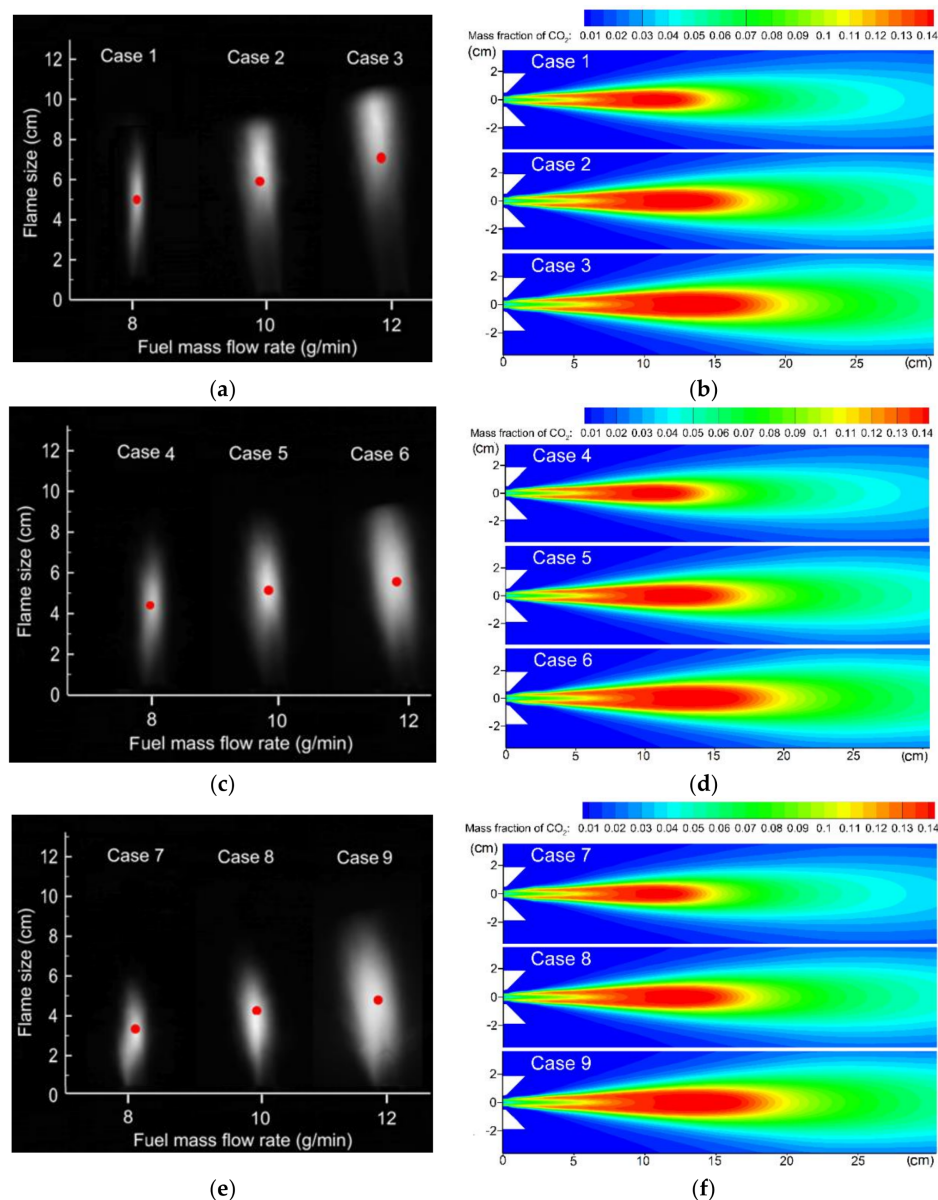
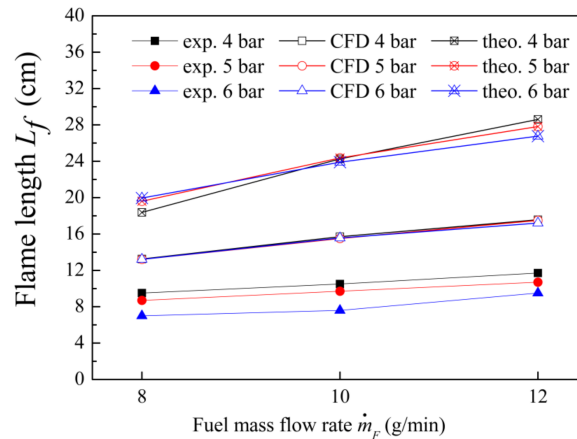


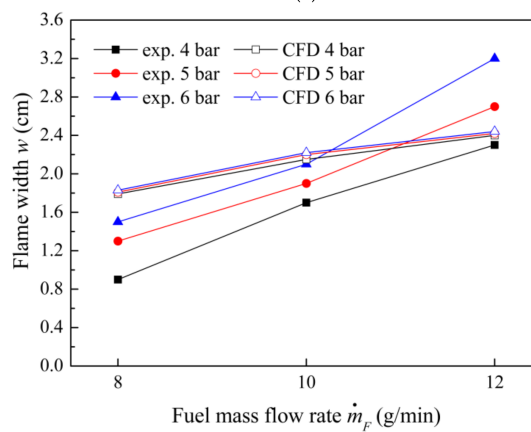
Figure 9. Flame shape for fuel mass flow rate under different combustor pressures: (a) experimental result at $P = 4$ bar; (b) CFD result at $P = 4$ bar; (c) experimental result at $P = 5$ bar; (d) CFD result at $P = 5$ bar; (e) experimental result at $P = 6$ bar; (f) CFD result at $P = 6$ bar.

In Figure 10a, L_f increased with the increment in \dot{m}_F at a fixed P for experimental, CFD, and theoretical results. All three had a linear relation with \dot{m}_F ; this phenomenon was also observed in previous research for turbulent swirl flames [13]. The increasing trend of L_f can be primarily attributed to the enhanced axial diffusion of the fuel. Moreover, more ambient air needs to be entrained to reach stoichiometric proportions. Both numerical and theoretical solutions gave a good prediction of the variation trend of L_f although the values were overestimated to some extent. The enlargement of

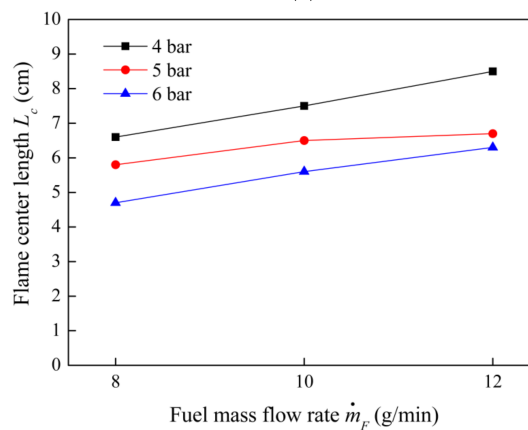
theoretical L_f is primarily due to the decreased f_s of the fuel mixture, which is caused by growing methane, according to Equations (4) and (5). Theoretical L_f was almost double the measured L_f , this difference mainly resulted from the swirl influences, since the addition of swirl can shorten L_f significantly in comparison to the flame with no swirl, as mentioned earlier [13]. However, swirl effect is not contained in Equation (5). Consequently, the present result estimated with Equation (5) is greater than the experimental one by a factor of two.



(a)



(b)



(c)

Figure 10. Flame size and position for fuel mass flow rate under different combustor pressures: (a) Flame length; (b) flame width; (c) flame position.

To consider the swirl effects on flame length, a coefficient could be supplemented as a swirl factor S_f in Equations (5) and (6) to apply them for swirl flames, i.e., Equations (10) and (11)

For a swirl buoyancy-controlled regime, $Fr_f < 5$

$$L_f = 13.5S_f \frac{Fr_f^{2/5}(\rho_e/\rho_\infty)^{1/2}d_j}{(1 + 0.07Fr_f^2)^{1/5}f_s} \quad \text{for } Fr_f < 5 \quad (10)$$

For a swirl momentum- controlled regime, $Fr_f \geq 5$

$$L_f = 23S_f \frac{(\rho_e/\rho_\infty)^{1/2}d_j}{f_s} \quad \text{for } Fr_f \geq 5 \quad (11)$$

The value for swirl factor S_f depends upon the specific swirl flames and could be determined by particular approaches, e.g., measuring flame lengths with swirl and no swirl for a wide range of operating conditions, such as the method in reference [13], all which are beyond the scope of the present article. In the current experimental situation, this factor seems to be approximately 0.5, with which the theoretical estimations are in good agreement with the test data.

Figure 10b indicates that flame width increased with \dot{m}_F at a fixed P for both experimental and CFD results. Since fuel flows along the flame axis and diffuses radially outward, while the air diffuses radially inward, increasing the fuel enlarges the radial position where f_s is achieved, and thus a wider flame is produced. The slope of the CFD results is smaller than the experimental ones, which may due to the simplicity of the one-step reaction mechanism in calculating flame width. Figure 10c shows the variation in flame position; as \dot{m}_F increased at a given P , the experimental flame center length also increased, this means that the flame moved further downstream, which corresponds to the variation of the flame length.

4.3. Effects of Combustor Pressure

It also can be seen in Figure 9, as the combustor pressure P increased at a given \dot{m}_F , the experimental flame shape became shorter and wider, this phenomenon was also observed in [23]. It could be associated with the declined axial diffusion, and enhanced radial diffusion of the fuel at higher P . The measured flame length diminished with the increment of P at a fixed \dot{m}_F , as displayed in Figure 11. This trend was also found in [29], where it was pointed out that L_f is proportional to $P^{-2/3}$, i.e., Equation (12), obtained by introducing the perfect gas state relation Equation (13) in Equation (14).

$$L_f \propto P^{-2/3} \quad (12)$$

$$\rho_\infty = \frac{P}{R_g T_\infty} \quad (13)$$

$$\frac{L_f}{d_j} = \left[\frac{Q}{\rho_\infty C_{p\infty} T_\infty g^{1/2} d_j^{2/5}} \right]^{2/3} \quad (14)$$

where Q is the heat release rate, $C_{p\infty}$ is the specific heat.

The curves in Figure 11 correspond to the fitting results under various fuel mass flow rates using power function $y = ax^b$. Values for exponent b for $\dot{m}_F = 8$ g/min, 10 g/min, 12 g/min are -0.7 , -0.73 , -0.5 respectively, which approaches the exponent $-2/3$ in Equation (12).

Figure 10 also shows that experimental flame width increased with the increment of P , and the flame position moved upstream at higher pressure. However, the numerical L_f and w remained consistent as P increased; CFD prediction did not capture the effect of P . Theoretical L_f showed a different varying trend with the increase of P for different \dot{m}_F .

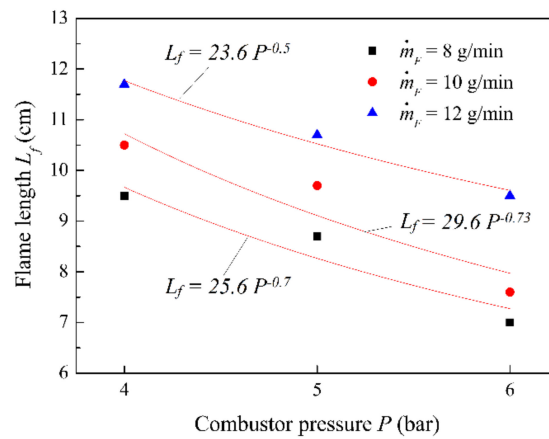


Figure 11. Measured flame length for combustor pressure under different fuel mass flow rates.

4.4. Effects of Primary Air Mass Flow Rate

Figure 12 displays the influence of primary air \dot{m}_{pri} on flame shape. As mentioned before, \dot{m}_{pri} increases with the increase of total air, and $\dot{m}_{pri} = 0.05 \dot{m}_A$. It can be seen that the experimental flame zone decreased gradually with the increment in \dot{m}_{pri} and the flame volume became smaller. The CFD flame appearance had the same decreasing trend as the experimental result.

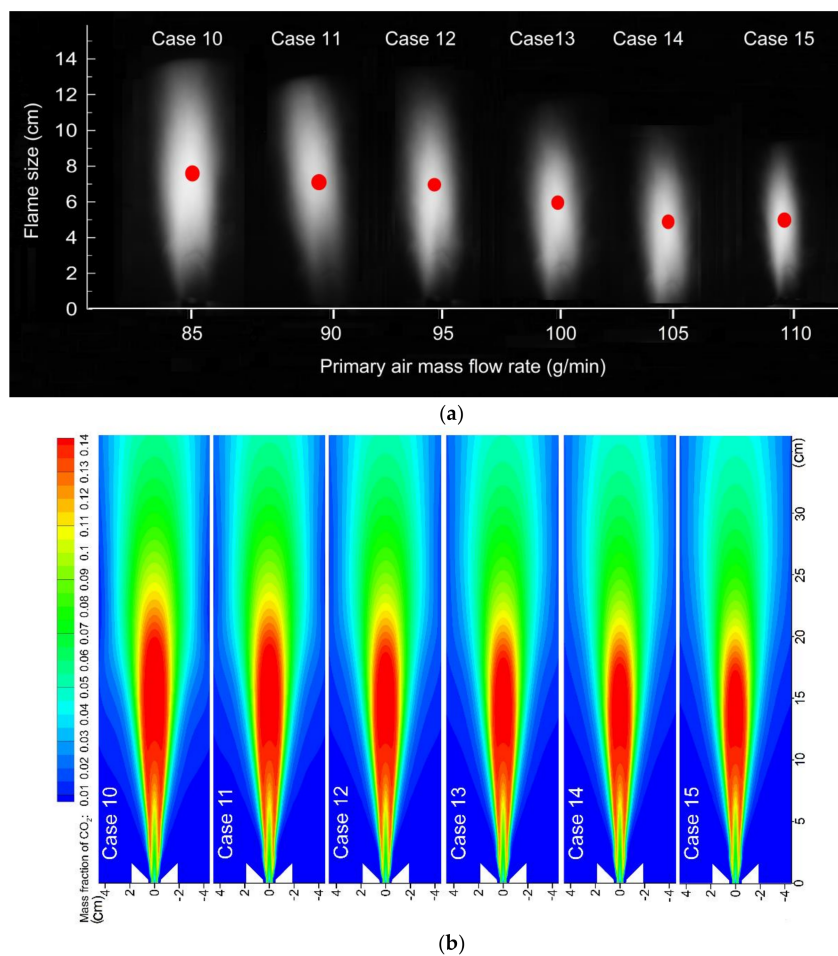
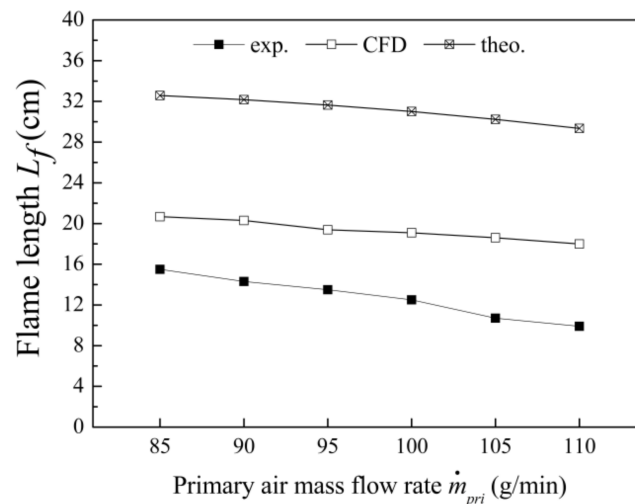


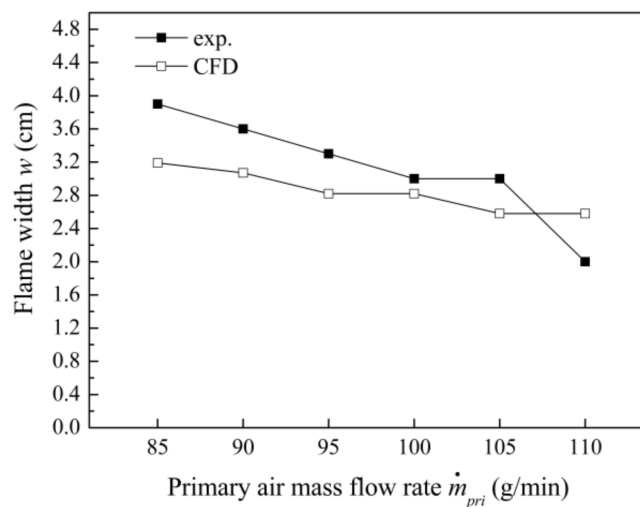
Figure 12. Flame shape for primary air mass flow rate (a) experimental result; (b) CFD result.

A shorter flame length was observed at higher primary air condition as shown in Figure 13a. L_f diminished with the increase in the primary air for measurement. This phenomenon is mainly attributed to the reduced air entrainment required for diluting the fuel to stoichiometric proportions. A similar result was stated in previous research [30], which measured the flame length for the fuel added with various quantities of air before combustion. Here, considering the primary air in the present experiment as the premixing air of [30], although the primary air does not mix with the fuel entirely as premixing air due to a short mixing distance, then from a qualitative level, the effect of both on flame length is analogous. CFD simulation predicted the diminishing trend of L_f correctly with a nearly equivalent slope, despite some discrepancies in values. The theoretical L_f also showed a consistent decreasing trend as the measured L_f , according to Formula (5). This decreasing L_f can be explained by increasing f_s as the primary air becomes larger. However, the values for theoretical L_f were almost twice the measured L_f , this difference is due to the swirl effects, as mentioned above.

Figure 13b illustrates the relation between flame width w and primary air \dot{m}_{pri} . Simulation results agreed well with experimental data; both showed a decrease in w when \dot{m}_{pri} increased. Diminishing w results from the reduced radial entrained air required to produce the flame surface. In Figure 13c, the experimental flame center length L_c diminished with increasing \dot{m}_{pri} , which indicates that the flame position moved upstream for larger \dot{m}_{pri} .

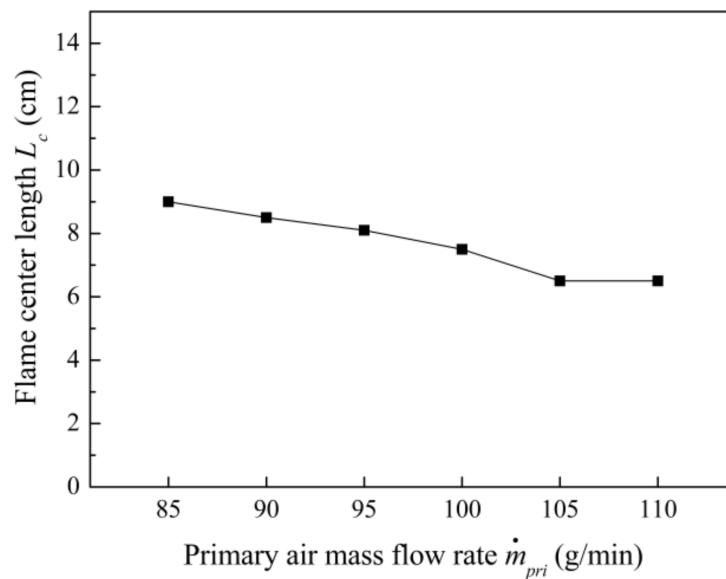


(a)



(b)

Figure 13. Cont.

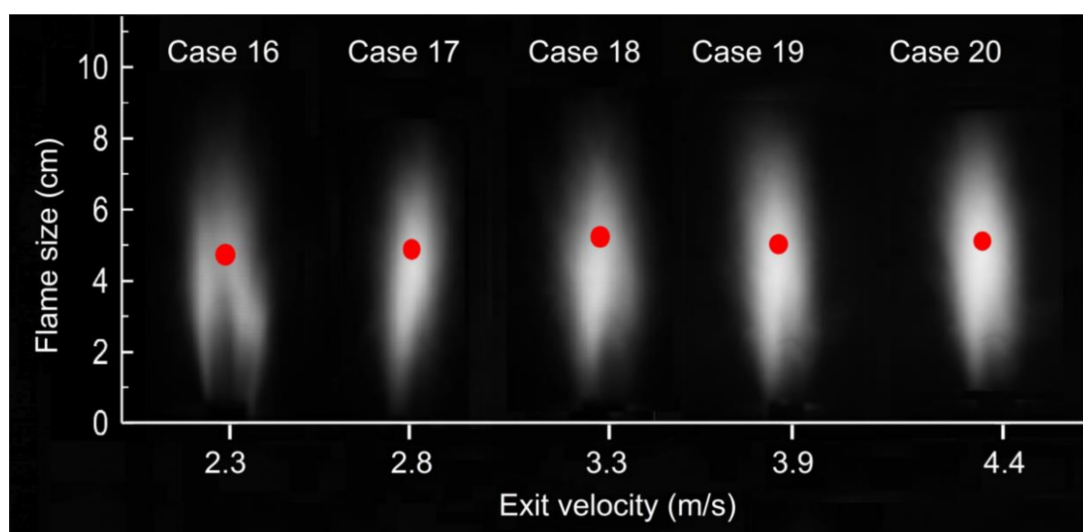


(c)

Figure 13. Flame size and position for primary air mass flow rate: (a) Flame length; (b) flame width; (c) flame position.

4.5. Effects of Nozzle Exit Velocity

Figure 14 displays the variation in flame shape with an increase in nozzle exit velocity v_e at a nearly fixed \dot{m}_{pri}/\dot{m}_F . Good agreement was observed in the trends of flame appearance versus v_e between experimental images and the CFD solutions. Both illustrate that the flame zone remained unchanged with increasing v_e , in other words, the flame volume did not obviously change. This can be attributed to the simultaneously increasing \dot{m}_F and \dot{m}_{pri} with $\dot{m}_{pri}/\dot{m}_F = \text{constant}$. On the one hand, increasing \dot{m}_F is conducive to the enlargement of the flame zone, as discussed in Section 4.2. However, on the other hand, increasing \dot{m}_{pri} is contributive to the reduction of flame volume, as stated in Section 4.4. Both effects seem to cancel each other out. As a result, flame shape and size remain nearly unchanged.



(a)

Figure 14. Cont.

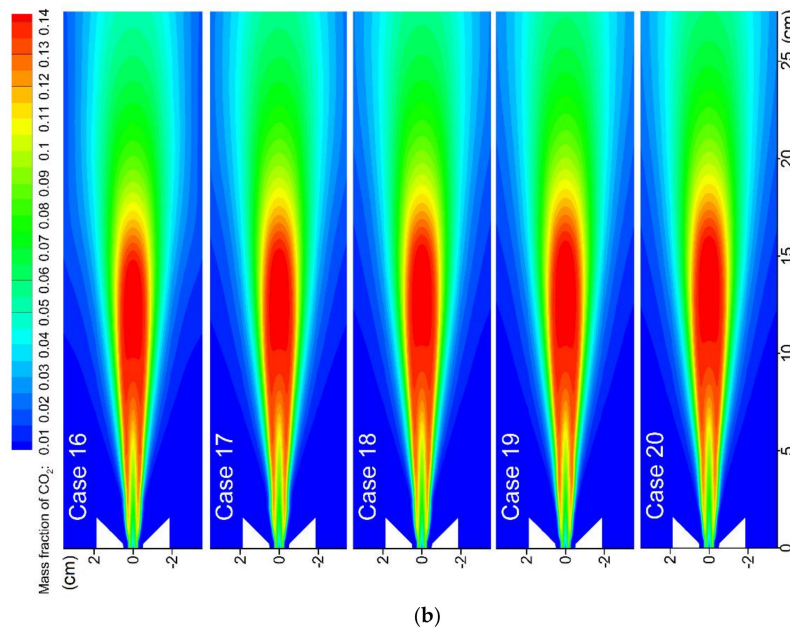


Figure 14. Flame shape for gas velocity: (a) Experimental result; (b) CFD result.

The result in Figure 15a indicates that flame length remained almost unchanged for the experimental data. Since f_s was nearly unchanged as v_e increased at a given \dot{m}_{pri}/\dot{m}_F , as displayed in Table 2, consequently, according to Equation (5), L_f remained unchanged. The numerical and theoretical methods gave good estimations of the variation trend of L_f , nevertheless, some deviations of values were observed. The difference between theoretical and experimental L_f is also attributed to swirl influence.

Figure 15b shows a rise and fall in flame width w with increasing v_e for the experimental case; this could have resulted from the flame instabilities. CFD w showed a slight fluctuation as v_e increased, a small deflection is found between the numerical value and experimental value. Experimental flame center length L_c in Figure 15c did not vary with an increase in v_e basically, which implies that the flame position remained unchanged.

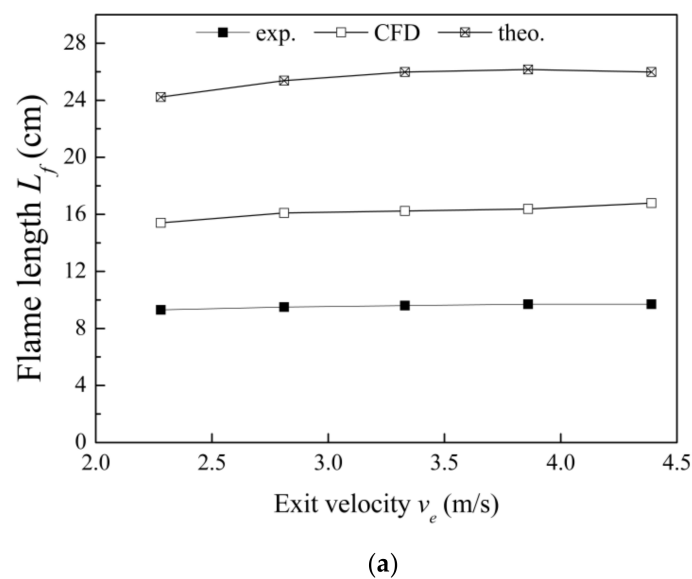
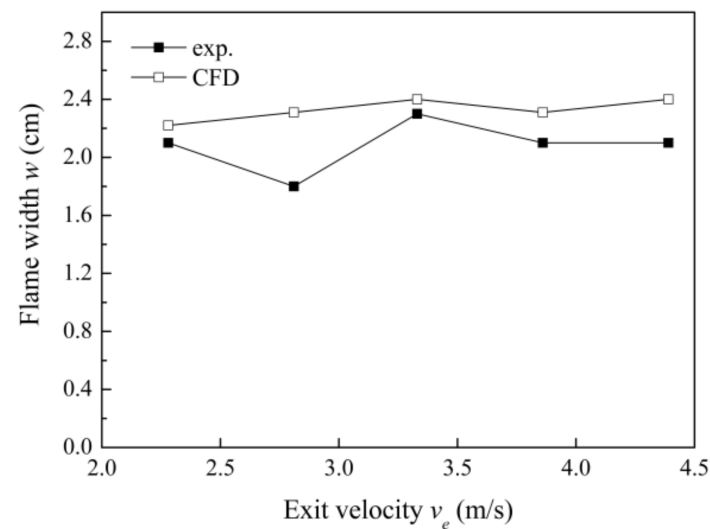
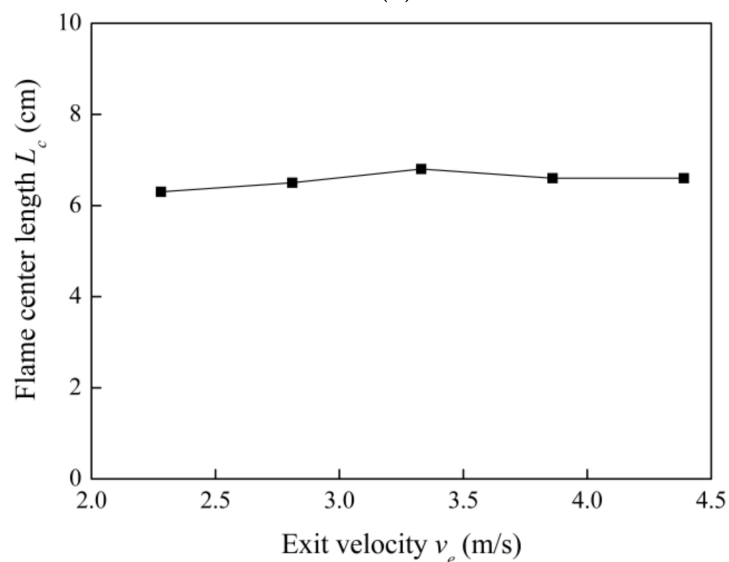


Figure 15. Cont.



(b)



(c)

Figure 15. Flame size and position for gas velocity: (a) Flame length; (b) flame width; (c) flame position.

4.6. Flame Size for Primary Air to Fuel Ratio

In order to consider the effects of the diverse operating conditions collectively, including the influences of \dot{m}_F , \dot{m}_{pri} , and v_e at the same combustion pressure, the results of Cases 4–6 and 10–20 are plotted in Figure 16, with a common abscissa \dot{m}_{pri}/\dot{m}_F .

It can be seen in Figure 16, that the measured L_f generally decreases with increment of \dot{m}_{pri}/\dot{m}_F , due to the reduced air entrainment required to dilute the fuel to stoichiometric proportions. The CFD results successfully captured the L_f variation trends, the difference between values for experiment and numerical simulation is reasonable. The theoretical equation also provided good estimation of the variation in L_f ; theoretical L_f decreased with increase in \dot{m}_{pri}/\dot{m}_F since f_s increased with the increment in \dot{m}_{pri}/\dot{m}_F , as shown in Table 2. However, the values for theoretical L_f were approximately twice the experimental L_f ; this difference is attributed to swirl impacts which were not involved in the theoretical formula.

The measured flame width w also showed a decreasing tendency as \dot{m}_{pri}/\dot{m}_F increased, due to the decreased radial air entrainment required to produce the flame zone. The CFD prediction on w

was in good agreement with experimental data. The flame center length L_c for the measured result diminished with an increment in \dot{m}_{pri}/\dot{m}_F , which indicates that the flame moved upstream; the flame position moved closer to the nozzle as \dot{m}_{pri}/\dot{m}_F increased.

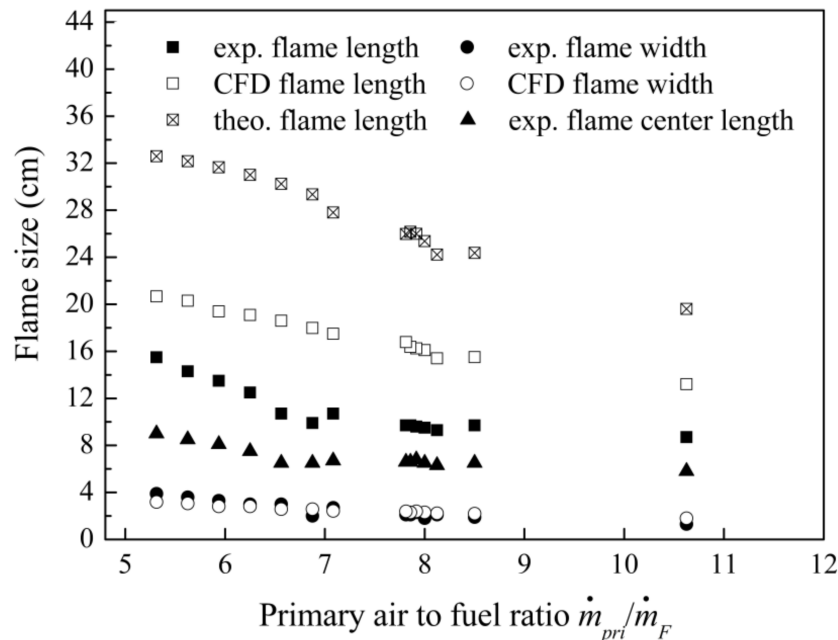


Figure 16. Flame size for primary air to fuel mass flow rate ratio.

5. Conclusions

The flame zone for a high-pressure turbulent non-premixed swirl flame was experimentally measured at various operating conditions. Meanwhile, a 2D CFD simulation was performed to predict the flame dimensions, and a theoretical calculation was carried out to estimate the flame length. This work attempts to provide measured information, numerical simulation, and theoretical calculation on flame shape and size for a high-pressure turbulent non-premixed swirl flame. It also helps in understanding flame geometric properties. The main findings of the present paper include:

- (1) As fuel mass flow rate \dot{m}_F increased, the flame shape became longer and wider, flame length increased and had a linear relation with \dot{m}_F . This is attributed to the enhancement in the axial diffusion of fuel and the increase in requirement of ambient air entrainment for diluting the fuel to stoichiometric proportions.
- (2) As combustor pressure P increased, the flame shape shortened and widened; flame length decreased and had a power relation with P . This probably resulted from declined axial diffusion and enhanced radial diffusion of the fuel at higher P .
- (3) As primary air mass flow rate \dot{m}_{pri} increased, the flame shape became shorter and narrower. The phenomenon is mainly caused by reduced air entrainment required to achieve stoichiometric proportions.
- (4) As the nozzle exit velocity v_e increased, flame length and width remained unchanged basically. This is mainly due to the concurrently increasing \dot{m}_F and \dot{m}_{pri} , with \dot{m}_{pri}/\dot{m}_F nearly being constant, the two effects are opposite and seem to cancel each other out.
- (5) In order to consider the effects of different operating conditions at the same combustor pressure collectively, the influences of \dot{m}_F , \dot{m}_{pri} and v_e were plotted together versus \dot{m}_{pri}/\dot{m}_F . As \dot{m}_{pri}/\dot{m}_F increased, flame length and width generally diminished, which is attributed to the reduction of air entrainment.

- (6) CFD provided decent prediction of the varying trends of flame shape and size, although some deviations were observed, which indicates that the present simulation is a reliable prediction tool for calculating the approximate flame shape and size.
- (7) The theoretical flame length also showed correct estimation of the varying trends. The difference between theoretical and experimental flame length is due to the influence of swirl; to consider swirl effects, a swirl factor is proposed to be added to the original equation.

Acknowledgments: This research was supported by Beijing Natural Science Foundation (Grant No. 3162030).

Author Contributions: Zhongya Xi and Zhongguang Fu conceived and designed the experiments; Zhongya Xi, Xiaotian Hu and Yibo Jiang performed the experiments; Zhongya Xi and Xiaotian Hu analyzed the data; Syed Waqas Sabir contributed reagents/materials/analysis tools; Zhongya Xi wrote the paper.

Conflicts of Interest: The authors declare no conflict of interest.

References

1. Turns, S.R. Laminar diffusion flames. In *An Introduction to Combustion: Concepts and Applications*; McGraw-Hill: New York, NY, USA, 2000; p. 315. ISBN 0677026900.
2. Sunderland, P.B.; Mendelson, B.J.; Yuan, Z.G.; Urban, D.L. Shapes of buoyant and nonbuoyant laminar jet diffusion flames. *Combust. Flame* **1999**, *116*, 376–386. [[CrossRef](#)]
3. Lin, K.C.; Faeth, G.M.; Sunderland, P.B.; Urban, D.L.; Yuan, Z.G. Shapes of nonbuoyant round luminous hydrocarbon/air laminar jet diffusion flames. *Combust. Flame* **1999**, *116*, 415–431. [[CrossRef](#)]
4. Joo, S.; Yoon, J.; Kim, J.; Lee, M.; Yoon, Y. NO_x emissions characteristics of the partially premixed combustion of H₂/CO/CH₄ syngas using artificial neural networks. *Appl. Therm. Eng.* **2015**, *80*, 436–444. [[CrossRef](#)]
5. Yoon, J.; Kim, M.K.; Hwang, J.; Lee, J.; Yoon, Y. Effect of fuel-air mixture velocity on combustion instability of a model gas turbine combustor. *Appl. Therm. Eng.* **2013**, *54*, 92–101. [[CrossRef](#)]
6. Figura, L.; Lee, J.G.; Quay, B.D.; Santavicca, D.A. The Effects of Fuel Composition on Flame Structure and Combustion Dynamics in a Lean Premixed Combustor. In *Proceedings of the ASME Turbo Expo 2007: Power for Land, Sea, and Air*, Montreal, QC, Canada, 14–17 May 2007; pp. 181–187. [[CrossRef](#)]
7. Hottel, H.C. Burning in laminar and turbulent fuel jets. *Symp. Combust.* **1953**, *4*, 97–113. [[CrossRef](#)]
8. Hawthorne, W.R.; Weddell, D.S.; Hottel, H.C. Mixing and combustion in turbulent gas jets. In *Symposium on Combustion and Flame and Explosion Phenomena*; Elsevier: New York, NY, USA, 1949; Volume 3, pp. 266–288.
9. Wohl, K.; Gazley, C.; Kapp, N. Diffusion flames. In *Symposium on Combustion and Flame and Explosion Phenomena*; Elsevier: New York, NY, USA, 1949; Volume 3, pp. 288–300.
10. Becker, H.A.; Liang, D. Visible length of vertical free turbulent diffusion flames. *Combust. Flame* **1978**, *32*, 115–137. [[CrossRef](#)]
11. Delichatsios, M.A. Transition from momentum to buoyancy-controlled turbulent jet diffusion flames and flame height relationships. *Combust. Flame* **1993**, *92*, 349–364. [[CrossRef](#)]
12. Blake, T.R.; McDonald, M. An examination of flame length data from vertical turbulent diffusion flames. *Combust. Flame* **1993**, *94*, 426–432. [[CrossRef](#)]
13. Chen, R.H.; Driscoll, J.F. The role of the recirculation vortex in improving fuel-air mixing within swirling flames. *Symp. Combust.* **1989**, *22*, 531–540. [[CrossRef](#)]
14. Peters, N.; Götting, J. Scaling of buoyant turbulent jet diffusion flames. *Combust. Flame* **1991**, *85*, 206–214. [[CrossRef](#)]
15. Røkke, N.A.; Hustad, J.E.; Sønju, O.K. A study of partially premixed unconfined propane flames. *Combust. Flame* **1994**, *97*, 88–106. [[CrossRef](#)]
16. Mei, Z.; Mi, J.; Wang, F.; Zheng, C. Dimensions of CH₄-Jet Flame in Hot O₂/CO₂ Coflow. *Energy Fuel* **2012**, *26*, 3257–3266. [[CrossRef](#)]
17. De Giorgi, M.G.; Sciolti, A.; Campilongo, S.; Ficarella, A. Flame structure and chemiluminescence emissions of inverse diffusion flames under sinusoidally driven plasma discharges. *Energies* **2017**, *10*, 334. [[CrossRef](#)]
18. Wang, Q.; Tang, F.; Liu, H.; Zhou, Z.; Palacios, A. Experimental investigation on the effect of reduced pressure on the combustion characteristics and flame height of gaseous fuel jets in parallel sidewalls. *Energy Fuel* **2017**. [[CrossRef](#)]

19. Bahadori, M.Y.; Stocker, D.P.; Vaughan, D.F.; Zhou, L.; Edelman, R.B. Effects of Buoyancy on Laminar, Transitional, and Turbulent Gas Jet Diffusion Flames. In *Modern Developments in Energy Combustion & Spectroscopy*; Pergamon Press: New York, NY, USA, 1993; pp. 49–66.
20. Choudhuri, A.R.; Gollahalli, S.R. Characteristics of hydrogen-hydrocarbon composite fuel turbulent jet flames. *Int. J. Hydrogen Energy* **2003**, *28*, 445–454. [[CrossRef](#)]
21. Yang, W.; Blasiak, W. Chemical flame length and volume in liquified propane gas combustion using high-temperature and low-oxygen-concentration oxidizer. *Energy Fuel* **2004**, *18*, 1329–1335. [[CrossRef](#)]
22. Kim, H.K.; Kim, Y.; Lee, S.M.; Ahn, K.Y. Studies on combustion characteristics and flame length of turbulent oxy-fuel flames. *Energy Fuel* **2007**, *21*, 1459–1467. [[CrossRef](#)]
23. Hu, L.; Wang, Q.; Delichatsios, M.; Tang, F.; Zhang, X.; Lu, S. Flame height and lift-off of turbulent buoyant jet diffusion flames in a reduced pressure atmosphere. *Fuel* **2013**, *109*, 234–240. [[CrossRef](#)]
24. Samaniego, J.-M.; Egolfopoulos, F.N.; Bowman, C.T. CO₂* Chemiluminescence in Premixed Flames. *Combust. Sci. Technol.* **1995**, *109*, 183–203. [[CrossRef](#)]
25. Lee, J.G.; Santavicca, D.A. Experimental Diagnostics for the Study of Combustion Instabilities in Lean Premixed Combustors. *J. Propuls. Power* **2003**, *19*, 735–750. [[CrossRef](#)]
26. Lee, J.; Kim, K.; Santavicca, D. A Study of the Role of Equivalence Ratio Fluctuations During Unstable Combustion in a Lean Premixed Combustor. In Proceedings of the 38th AIAA/ASME/SAE/ASEE Joint Propulsion Conference & Exhibit, Indianapolis, IN, USA, 7–10 July 2002.
27. Fluent Inc. *FLUENT 6.3 Theory Guide*; Fluent Inc.: Lebanon, NH, USA, 2006.
28. Magnussen, B.F.; Hjertager, B.H. On mathematical modeling of turbulent combustion with special emphasis on soot formation and combustion. *Symp. Combust.* **1977**, *16*, 719–729. [[CrossRef](#)]
29. Most, J.M.; Mandin, P.; Chen, J.; Joulain, P.; Durox, D.; Carlos Fernande-Pello, A. Influence of gravity and pressure on pool fire-type diffusion flames. *Symp. Combust.* **1996**, *26*, 1311–1317. [[CrossRef](#)]
30. Turns, S.R.; Myhr, F.H.; Bandaru, R.V.; Maund, E.R. Oxides of nitrogen emissions from turbulent jet flames: Part II-Fuel dilution and partial premixing effects. *Combust. Flame* **1993**, *93*, 255–269. [[CrossRef](#)]



© 2018 by the authors. Licensee MDPI, Basel, Switzerland. This article is an open access article distributed under the terms and conditions of the Creative Commons Attribution (CC BY) license (<http://creativecommons.org/licenses/by/4.0/>).